ARTICLE

Check for updates

Increased amplitude of atmospheric rivers and associated extreme precipitation in ultra-high-resolution greenhouse warming simulations

Arjun Babu Nellikkattil [1,2✉], June-Yi Lee [1,2,3✉], Bin Guan [4,5], Axel Timmermann [1,6], Sun-Seon Lee [1,6], Jung-Eun Chu [7] & Danielle Lemmon [1,6,8]

Atmospheric rivers play an integral role in the global water cycle, but predicting their future changes remains uncertain due to inter-model and inter-detection-method differences. Using ultra-high-resolution Community Earth System Model simulations and a novel detection algorithm based on geometric shape extraction, we quantify global changes in atmospheric rivers and the associated precipitation events in response to doubling and quadrupling of atmospheric CO_2 concentrations. We find that, atmospheric rivers are projected to become more frequent and more likely to be associated with extreme precipitation events, increasing their contribution to global mean precipitation. While the water vapor transport within these structures follow Clausius-Clapeyron scaling, the changes in maximum precipitation intensity resemble other saturated atmospheric environments like tropical cyclone cores. The increased amplitude of atmospheric rivers and the associated increase in mean and extreme precipitation have important implications for future water management and adaptation policies.

[1] Center for Climate Physics, Institute for Basic Science, Busan, South Korea. [2] Department of Climate System, Pusan National University, Busan, South Korea. [3] Research Center for Climate Sciences, Pusan National University, Busan, South Korea. [4] Joint Institute for Regional Earth System Science and Engineering, University of California, Los Angeles, CA, USA. [5] Jet Propulsion Laboratory, California Institute of Technology, Pasadena, CA, USA. [6] Pusan National University, Busan, South Korea. [7] Low-Carbon and Climate Impact Research Centre, School of Energy and Environment, City University of Hong Kong, Hong Kong, China. [8] American Association for the Advancement of Science, Science and Technology Policy Fellowship, Washington D.C., USA. ✉email: arjunbabun@pusan.ac.kr; juneyi@pusan.ac.kr

Atmospheric Rivers (ARs) are narrow, filament-like structures that transport large amounts of water vapor across the globe[1,2]. They often form ahead of the cold fronts of an extratropical cyclonic circulation accompanied by a low-level jet on the equatorward side and strong convection along the front, constituting large-scale cloud systems with persistent precipitation. ARs undergo vigorous upward motion along topographic barriers like mountains or coastlines where they make landfall, leading to torrential downpours. At any given instant, about four or five ARs per hemisphere provide much of the poleward water vapor transport across the midlatitudes[3]. When time-averaged, over 90% of the total annual poleward water vapor transport in the midlatitudes is controlled by ARs that account for only 10% of the total global surface area[4]. AR genesis and activity also modulate the global mean atmospheric energy budget via sensible and latent heat transports[5].

Understanding ARs and determining their response to greenhouse warming is extremely important as they play a fundamental role in global and regional hydroclimate[6]. From a global perspective, ARs account for up to 35% of the annual mean precipitation[7] and around 50% of the extreme precipitation and surface wind events in the midlatitudes[8]. Regionally, ARs substantially modulate mean and extreme precipitation along land-falling coastal regions, such as the U.S. west and east coasts[9–12], European west coast[13–15], South American coastline[16], and Australasia summer monsoon regions[17–20]. ARs also influence the intensity of snowfall and snowpack variability over many land-falling regions[21–24]. The mean hydroclimate over these areas are shaped by ARs in the present as well as past climates[25–27]. More recently, it has been found that ARs influence the ice melting in the polar regions and glaciers, owing to consistently strong precipitation and long-wave feedbacks associated with AR cloud cover. The complex interplay between ARs, clouds, and ice sheets leads to different outcomes in different regions, such as anomalous snow accumulation over East Antarctica[28], surface melting over West Antarctica[29], reduction of sea-ice in both the Antarctic and the Arctic[30,31], and extreme melting of Greenland ice sheet[32]. Thus, ARs play an important and intricate role in global and regional climate feedbacks.

Recent modeling efforts have advanced our understanding of the dynamics, forced responses, and impacts of ARs. These studies suggest that the frequency of ARs will increase, and their landfall locations will shift poleward in response to anthropogenic greenhouse warming[33,34]. Additionally, due to increases in atmospheric moisture, ARs are expected to carry more moisture and increase the associated likelihood of extreme precipitation, particularly over regions with elevated terrain[6,35–38]. While considerable progress has been made in the simulation, prediction, and projection of ARs using climate models, coarse-resolution models still have large biases in representing the spatio-temporal characteristics of ARs as well as their interaction with topographic features[39]. These model deficiencies are closely related to biases in the representation of midlatitude storm tracks and jet streams[40,41]. Although more work needs to be done to definitively conclude whether ARs are better represented in higher resolution models, AR frequencies are suggested to be highly influenced by the horizontal grid resolutions used in climate models[42]. For example, model simulations with higher horizontal resolutions are expected to represent more realistic precipitation patterns[43–45] and frontal-scale midlatitude air-sea interactions[46,47], thus better capturing the interactions between ARs and complex topography[6]. Moving forward in understanding AR dynamics and reliable projections, then, requires reconciling findings from both coarse and high-resolution modeling studies.

While developments in high-resolution modeling have much potential to advance our understanding of ARs, current scientific consensus on new findings is elusive as non-negligible differences in present and projected AR features have been attributed to fundamental differences between AR detection algorithms (ARDTs)[34,48,49]. The majority of pre-existing ARDTs use absolute or relative thresholds based on climate variables, such as integrated water vapor content (IWV) or integrated water vapor transport (**IVT**) (hereafter thresholds), along with few shape, size and location constraints to identify ARs in the present climate[50,51]. Studies on reanalysis data sets that use detection methods with absolute thresholds show a high concentration of ARs along the warm western boundary current region in the global oceans and an asymmetric distribution of ARs between the Northern and Southern Hemispheres[52–54]. By contrast, reanalysis studies that use thresholds relative to the mean state, as a function of space and time, show a more symmetric distribution of ARs between the two hemispheres and detect considerably more ARs over land[7,26,55,56]. Differences in results obtained between these two methods are likely attributable to the uneven spatial distribution of mean water vapor between hemispheres, which is inherently captured differently by absolute and relative thresholds. Even given the relative consistency between reanalysis data sets in representing present climate, as compared to historical model simulations, building consensus on AR characteristics is difficult as the analysis is extremely sensitive to ARDTs[49].

The sensitivity of results from AR analysis to ARDTs is even greater when estimating the changes in AR characteristics between various mean climate states, such as between different models and different climate change scenarios. Compared to interpreting AR characteristics in the present climate, analyzing projected AR changes in future climate becomes even more complicated as methods can be based on historical thresholds (i.e., absolute or fixed relative schemes) or based on mean state thresholds (i.e., relative schemes)[34]. For example, model studies that use methods based on historical thresholds tend to project ARs as much longer and wider, with small changes in mean strength and precipitation in response to greenhouse gas (GHG) warming[33,34]. Conversely, model studies using relative mean state thresholds tend to project ARs as greatly strengthened in both IVT and precipitation, with smaller changes in their length and width[57]. The proliferation of the number and type of ARDTs has led to multiplicitous and conflicting interpretations of projected changes, obscuring scientific consensus on AR characteristics in present and future climate.

To simplify the study of present and future AR changes, alternative methods without dependence on climate variable thresholds are being explored by the community, with some studies highlighting the potential benefits of machine learning or image processing techniques[58–60]. To develop a robust ARDT in mind, we use a methodology that reframes the basis of thresholds away from climate variables like **IVT** or IWV towards shape-based metrics that are not empirically derived from climate data, and thus may be less sensitive to underlying changes in climate mean states (see "Scalable Feature Extraction and Tracking (SCAFET)" in "Methods" section).

Considering the potential of high-resolution modeling to improve our understanding of ARs, and the conflicting AR analysis that appears to arise from **IVT** and IWV threshold-dependence, this study addresses externally forced changes in ARs and the associated precipitation in response to anthropogenic GHG warming using (1) ultra-high-resolution (UHR) fully coupled simulations, and (2) a novel detection method based on a local geometric shape extraction, namely Scalable Feature Extracting and Tracking (SCAFET)[61]. We analyze present-day (PD), CO_2 doubling (2CO2), and quadrupling (4CO2)

simulations from the UHR Community Earth System Model (CESM) version 1.2.2 with about 0.25° and 0.1° horizontal resolution for atmosphere and ocean, respectively[62]. See the "Methods" section for description of the data, model and methods used in this study. ARs within CESM UHR simulations and reanalysis are detected using SCAFET, and are validated against the observed features and the projected changes in AR characteristics from other studies (sections "ARs in the present climate simulation" and "AR responses to greenhouse warming"). Their role in inducing extreme precipitation is then discussed in the following section (see "Extreme precipitation associated with ARs").

Results

ARs in the present climate simulation. Using SCAFET, we compare the 20-year mean spatial distribution of daily AR frequency in the CESM UHR PD simulation with the observed high-resolution counterpart obtained from the European Centre for Medium-Range Weather Forecasts (ECMWF) Reanalysis Version 5 (ERA5). The CESM UHR PD simulation well captures the observed global distribution of the climatological AR frequency (Fig. 1a, b). The maximum values of the AR frequency are found along the storm track regions in the midlatitudes (contours in Fig. 1a, b). AR frequencies are also high over the warm western boundary currents and the currents' extensions throughout the year. These AR structures are associated with the frequent moving-extratropical cyclones (ECs) in that region. The integral role of ARs in regulating midlatitude water cycle is likewise observed in the CESM UHR PD and ERA5 datasets, where ARs account for a considerable portion of the precipitation (1d, e). ARs exhibit an equator to poleward migration during the respective summers for both hemispheres, and a pole to equatorward migration during the respective winters (Supplementary Fig. 1). Not only does the PD simulation analyzed with SCAFET captures the climatological AR frequency and the fraction of AR precipitation as in ERA5, but it is also comparable to the results derived from various other databases using a variety of ARDTs (see Fig. 9[7], Fig. 1[49], Supplementary Figs. 2 and 3).

As observed by recent studies, we find that the spatial pattern of mean AR frequency is largely insensitive to the spatial resolution of the simulations used[63,64] (see Supplementary Fig. 4). As the parameters used for AR detection in low resolution (LR) datasets are same as that with the high resolution (HR), this also demonstrates the ability of SCAFET to detect ARs from datasets with varying resolution. However, the HR simulations show a more realistic representation of the precipitation and convection characteristics compared to LR counterparts[65]. Consistent with these studies, the CESM UHR PD simulation presented here shows more accurate representation of the AR characteristics as compared to analogous LR simulations (Supplementary Fig. 5). The differences between HR and LR AR characteristics are considerable in the extreme attributes. Since extreme precipitation is an important facet of ARs, HR simulations and resolution-insensitive detection algorithms should be used in future studies into the mechanism and the impacts on extreme precipitation.

Whereas the overall patterns in AR frequency between SCAFET and other ARDTs are comparable, SCAFET tends to detect weaker ARs more than most canonical ARDTs and thus detects a higher overall AR frequency (see also Supplementary Figs. 2 and 3). The detection of a large number of weak ARs is expected, as the algorithm does not set a minimum threshold on **IVT**. AR-like objects are identified from the **IVT** fields by extracting ridge, and dome-shaped objects within the data. A scale-insensitive, bounded varibale called Shape Index (SI)[66] is used to segment the **IVT** field into various shapes. In essence, regions with SI > 0.375 will be labeled as ARs, given that they are precipitating, large, elongated and have a coherent vapor transport (see "Methods" for further details). Although the algorithm sets an absolute (independent of both space and time) threshold, unlike other ARDTs that sets absolute thresholds (Supplementary Figs. 2a–c), we get a hemispherically uniform distribution of ARs similar to ARDTs based on relative thresholds (Supplementary Figs. 2e–g). Thus, although the algorithm cannot theoretically define an AR, it puts forward a unique perspective in its detection. Excitingly, such a framework can be extended to the detection of other climate and weather features[61].
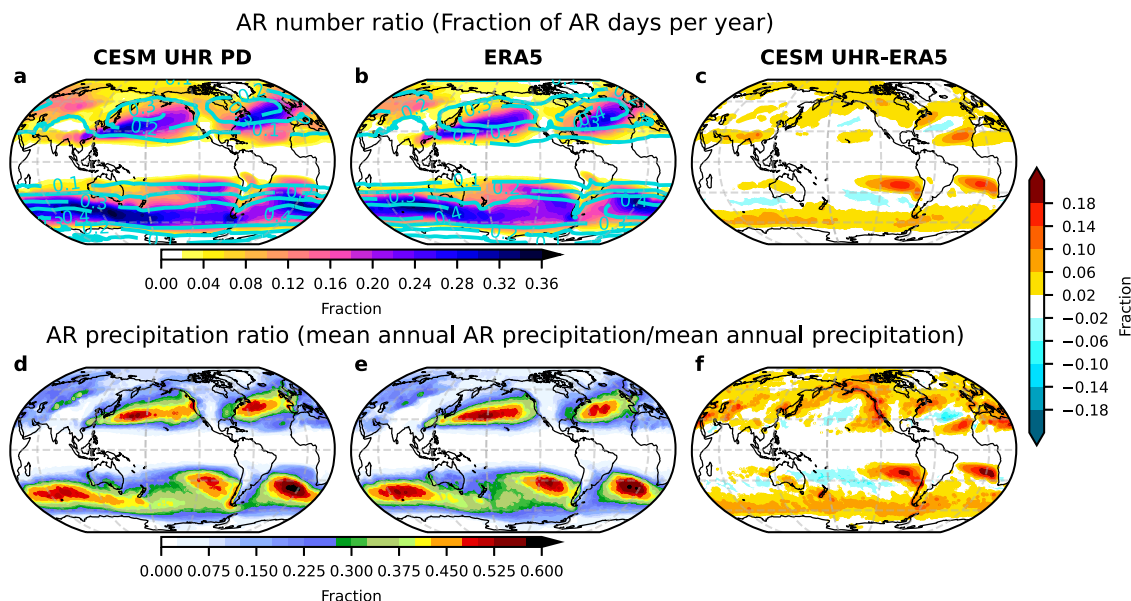

Fig. 1 The mean AR statistics in CESM ultra-high-resolution (UHR) PD simulation compared with ERA5 reanalysis. Fraction of AR days per year (nondimensional) in the CESM UHR PD simulation (**a**), ERA5 (**b**), and their difference (**c**), and the ratio of AR precipitation to annual mean precipitation (nondimensional) in the CESM UHR PD simulation (**d**), ERA5 (**e**), and their difference (**f**). The model climatology is calculated from the daily mean data of the last 20 years of the PD simulation, and the observed climatology is obtained for the 20 years of 2000–2019. The cyan contours in **a** and **b** show the column integrated eddy kinetic energy in Mega Joules (MJ).

The most notable difference between ERA5 and the CESM UHR PD simulation is the location of the maximum AR frequency and associated precipitation (Fig. 1c, f). This discrepancy could be due to model biases in the location and extent of the jet streams and associated storm tracks in the simulation (Supplementary Fig. 6). Despite minor inter-data and inter-detection-method differences, there is good agreement in AR characteristics between ERA5 and the CESM UHR PD simulation using SCAFET, and little divergence in this analysis from the other ARDTs (see Supplementary Figs. 2 and 3). The choice of the reanalysis datasets will not affect observed biases as detection of ARs is not sensitive to the absolute values of the **IVT** and is similar to relative threshold based ARDTs[63] (Supplementary Fig. 7).

The mean climatology of AR frequency exhibits considerable similarity to the means of other synoptic-scale weather systems such as storm tracks, warm conveyor belts (WCBs), ECs, and atmospheric fronts (AFs). Maximum AR frequencies are manifested on the equatorward side of active storm track regions (Fig. 1a, b contours). Storm track activity is directly proportional to the track density of ECs, and the starting and ending points of the WCBs match well with the genesis and lysis locations of the cyclones[67–69]. Also, the distribution of AFs tends to strongly correlate with the AR activity (see Fig. 2[70]). From a cyclone-centered view, ARs can be viewed as vestiges of a poleward moving extratropical storm[71,72], with robust co-occurrences and moderate correlations between AR and storm strength[73,74]. Connecting all these features, ARs are generally formed along the equatorward side of strong cyclonic circulations, extending from WCB genesis locations along with the warm sector of AFs. Importantly, the SCAFET framework well-captures this dynamic link between ARs and synoptic-scale features.

AR responses to greenhouse warming. By combining the novelty of both the CESM UHR simulations and the local geo-metric shape-based detection method, SCAFET, we aim to more reliably quantify the AR responses to GHG forcing. Our results indicate that changes in the 20-year mean of AR frequency under 2CO2 and 4CO2 relative to the PD simulation are highly regional (Fig. 2a, b). Overall, mean AR frequency manifests a robust linear response to increased GHG forcing. Over the jet exit regions in North Pacific, North Atlantic, and South Pacific, there is a sta-tistically significant reduction in the mean AR frequencies, though only for the 4CO2 scenario. The spatial patterns in the Southern Ocean, especially over the Southern Indian and Atlantic basins resemble a poleward shift in the mean AR frequencies. The Indian and East Asian monsoon regions display a slight poleward shift in the mean AR distributions. Large increases in AR fre-quency are also observed along the near-equatorial regions in North Pacific and North Atlantic, the southwestern part of North America, the northwestern part of Europe, and western Africa. A homogenous upsurge in AR frequencies can also be seen across the Arctic region, with pervasive influence on icesheet and sea ice dynamics across the domain. Other regions like Australia and Central Asia (east of the Caspian Sea) see large-scale reductions in AR activity. The global mean of AR frequency is projected to increase by about 6% and 12% in the 2CO2 and 4CO2 simulations, respectively, relative to the PD simulation. In line with previous studies, our findings indicate a general increase in the average frequency of ARs in response to GHG-induced warming, although notable regional reductions are observed.

Estimated global mean changes in AR frequency are consider-ably less than those cited in previous studies. For example, one study using historical thresholds projected an increased global mean AR frequency of about 50% by the end of the 21st century

in the RCP 8.5 scenario[33]. Application of the same detection method using historical thresholds for the CESM simulations quantifies a 42% and 61% increase in global mean AR frequency in the 2CO2 and 4CO2 simulations, respectively, exhibiting projections that are more than 5 times larger than the SCAFET-derived estimation (Supplementary Fig. 8a, b). If the same detection method is applied with the mean state thresholds (not shown), the increase in global mean AR frequency is estimated to be 11% and 19% in the 2CO2 and 4CO2 simulations, respectively, which is still considerably larger than the SCAFET-derived estimation of 6% and 12%. The large discrepancy in results between SCAFET and canonical ARDTs may in part be because SCAFET is not affected by the homogenous increase in **IVT** from global warming, while threshold-based detection methods are fundamentally affected. Utilizing TempestExtremes[54] to calculate the responses of ARs to GHG warming shows results that are closer to the changes obtained from SCAFET (Supplementary Fig. 8c, d). This is because, to detect ARs, TempestExtremes applies thresholds on the Laplacian of the **IVT** field, which by definition is the divergence of the spatial gradient and is thus similarly insensitive to homogeneous mean state increases in **IVT**. By contrast, ARDTs that use historical or present day **IVT** or IWV thresholds identifies larger AR areas as they do not account for a future mean state that has ubiquitously higher specific humidity[34]. By increasing the minimum thresholds for **IVT** or precipitation in the SCAFET, similar patterns of AR frequency changes can be observed compared to conventional ARDTs (Supplementary Fig. 9). Ultimately, the choice of AR detection method depends on the specific research question being addressed.

Reconciling the patterns of projected AR frequency changes between modeling studies is difficult not only because of different threshold-dependent ARDTs but also because AR projections depend on variable thermodynamic and dynamic physical quantities, like specific humidity and wind speed. Modeling studies have shown that a 1 °C increase in global mean temperature corresponds to about a 7% increase in water vapor content and CESM UHR simulations also show that the lower tropospheric mean specific humidity (1000 hPa to 700 hPa) globally increases by about 7.3% and 8% globally per 1 °C global warming in 2CO2 and 4CO2 scenarios, respectively[75]. The changes in wind magnitude and direction are less certain and are dependent on the regional and model characteristics. A combination of these climatological changes modulates the the spatial pattern of **IVT**, and by extension the spatial pattern of AR frequency. To separate out the influence of humidity increases and wind changes, we split total **IVT** changes (Δ**IVT**) into the thermodynamic ($\int \overline{\mathbf{V}}\Delta q dp$) and dynamic ($\int q\Delta\overline{\mathbf{V}}dp$) compo-nents, hereafter **TIVT** and **DIVT** respectively (see the "IVT decomposition" in "Methods" for complete decomposition of **IVT**). By separating the thermodynamic and dynamic compo-nents, we explicitly show how SCAFET delineates projected AR characteristics from the underlying dynamics and mean state trends that modulate projected changes in AR frequency.

To demonstrate how **TIVT** and **DIVT** affect the mean **IVT** and hence the distribution of AR frequency, we take the vector projection of **TIVT** and **DIVT** onto mean **IVT** from PD (Fig. 2e–h). In linear algebra the vector projection of a vector $\overrightarrow{a}$ onto another nonzero vector $\overrightarrow{b}$ is defined as $a \cdot b/|b|$. Positive values of the scalar product indicate that the changes act to reinforce the mean circulation in PD while negative values imply that the changes are in the opposite direction of the mean circulation and result in the weakening of the total transport. ARDTs that are based on historical or relative thresholds estimate AR frequency changes that are sensitive to both components, and
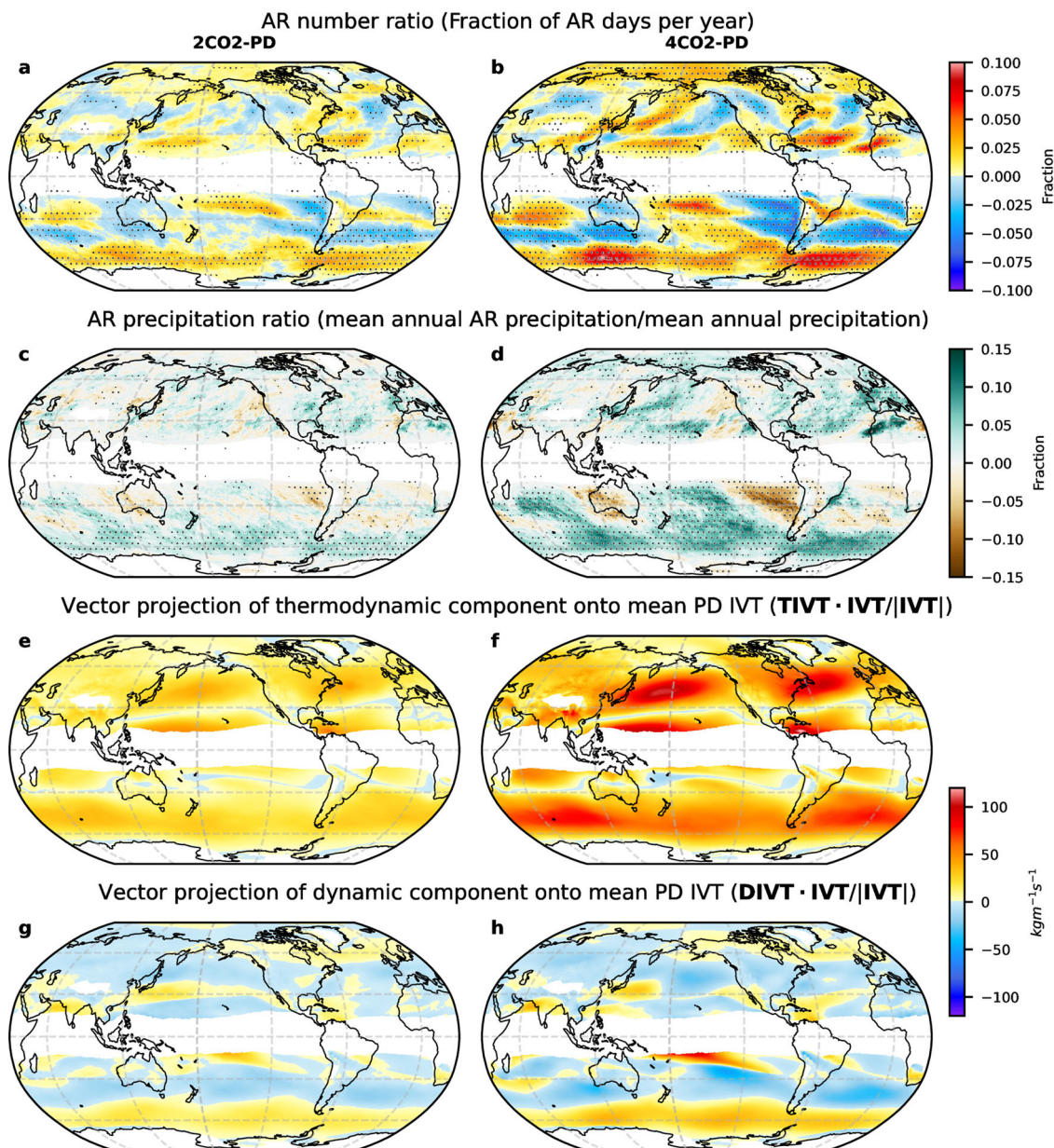
Fig. 2 Projected changes in AR characteristics, thermodynamic and dynamic components of integrated water vapor transport (IVT). Future changes in the annual fraction of AR days (**a**, **b**), AR precipitation to annual mean precipitation ratio (**c**, **d**) from 2CO2 (**a**, **c**) and 4CO2 (**b**, **d**) experiments in comparison to PD. Stippling in **a–d** denotes significant changes at $\alpha = 0.05$ level in a two-tailed t-test ($n = 20$). The vector projection of thermodynamic (**e**, **f**), and dynamic (**g**, **h**) components onto the mean **IVT** from PD are shown as shading.

thus AR frequency is largely increased following **TIVT** (Supplementary Fig. 8a, b). However, SCAFET is more responsive to changes in **DIVT**, similar to other ARDTs that either use a relative or second-derivative threshold (Supplementary Fig. 8c, d). Regions where both **TIVT** and **DIVT** act to strengthen the mean circulation show the largest increase in AR frequency, as in the Southern Ocean (Fig. 2e–h). In most regions where the **DIVT** changes are opposing the **TIVT** changes, AR frequency often seems to follow the mean **DIVT**, particularly over the midlatitudes. As the wind response to GHG warming is highly model dependent, mean AR frequencies obtained using SCAFET may vary between models (Supplementary Fig. 10). Examining the zonal and meridional components separately also tells the same story in that AR frequency changes are modulated by **DIVT**, though the meridional components are inessential in

explaining the overall pattern (Supplementary Figs. 11–14). Compared to other ARDTs, AR frequency is more modulated by **DIVT** in our scheme due to the fact that SCAFET identifies regions with local maxima in **IVT** regardless of its absolute value. In other words, SCAFET by construct not only identifies regions with high water vapor content but also the low level jet structure associated with it, which is represented by **DIVT**.

The precipitation changes associated with ARs are consistent with the changes in AR frequency (Fig. 2c, d). Globally, the contribution of AR precipitation to mean annual precipitation increases by 6%(2.4%/°C) and 15%(3%/°C) in 2CO2 and 4CO2 scenarios respectively, which was also seen in previous studies[76]. The greatest increases in AR precipitation occur over high and midlatitudes (Fig. 2c, d), closely following the projected changes in total precipitation[62] (Supplementary Fig. 15).
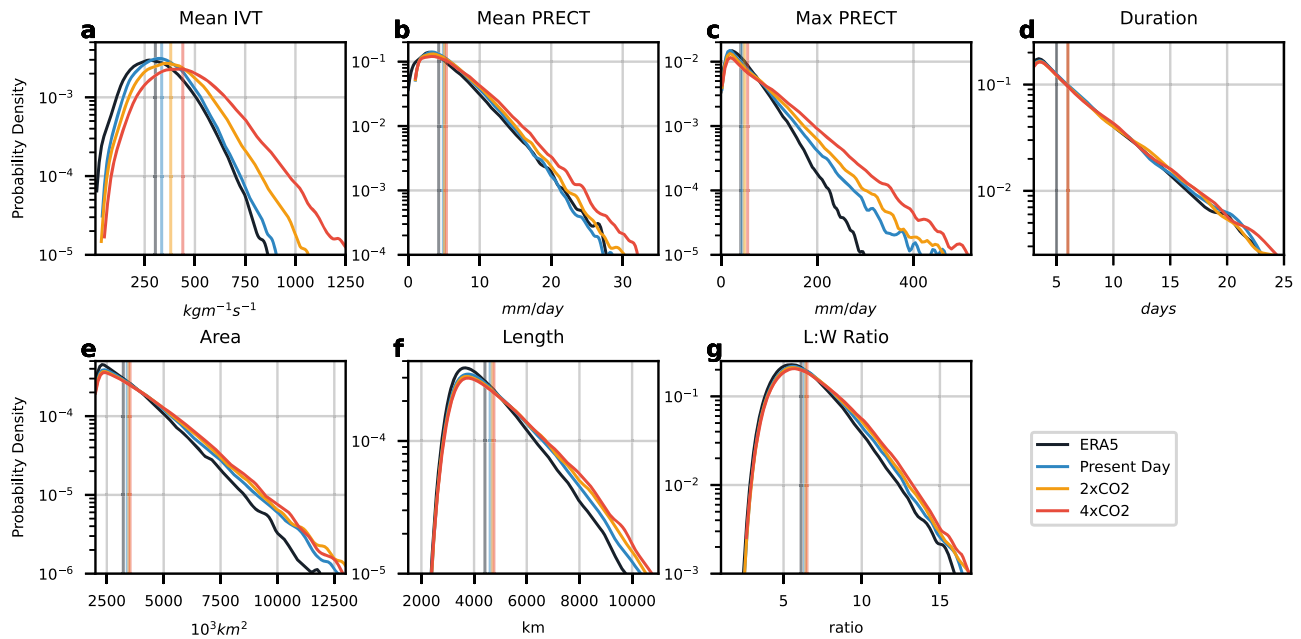
Fig. 3 Changes in the distribution of AR properties. Probability density function of AR (**a**) mean integrated water vapor transport (**IVT**), (**b**) mean precipitation (PRECT), (**c**) maximum precipitation, (**d**) duration, (**e**) area, (**f**) length, and (**g**) the ratio of length to width for ERA5 (black), PD (blue), 2CO2 (orange), and 4CO2 (red). The vertical lines represent the median value of the distribution. Y-axis for all plots are represented in log scale.

Additionally, we find that ARs are projected to become stronger by 15%(6%/°C) and 34%(7%/°C) in 2CO2 and 4CO2 simulations respectively, consistent with the Clausius-Clapeyron scaling[75] (Fig. 3a). The mean precipitation within the ARs increases by 4%(1.6%/°C) and 10%(2%/°C) congruent with the hydrological sensitivity estimated from other coupled climate simulations[77] (Fig. 3b) while the maximum precipitation within ARs shows amplification by 12%(5%/°C) and 30%(6%/°C) for 2CO2 and 4CO2 scenarios, respectively (Fig. 3c). These changes in maximum precipitation within ARs are similar to responses observed in other saturated atmospheric environments like tropical cyclones[78]. Although the changes in mean AR precipitation is dependent on the AR boundary which in turn is highly sensitive to the choice of ARDT, maximum AR **IVT** and precipitation are largely insensitive to the detection methods used. AR duration shows an extension of 1.6% and 2.3% in 2CO2 and 4CO2 scenarios (Fig. 3d). Moreover, ARs tend to become 1.5% and 3% longer, bigger, and more elongated in 2CO2 and 4CO2 simulations (Fig. 3e–g). However, these geometric parameters are highly sensitive to the ARDT used. For instance, results obtained using historical thresholds show larger increases in length, width, and area with only moderate changes in mean AR **IVT** and precipitation[34]. Results obtained using mean state thresholds show moderate changes in geometric parameters and a generous increase in **IVT**, similar to our results[57]. Local shape-based methods like SCAFET have the potential to reduce the ambiguity in projected changes of ARs arising from IWV or **IVT** threshold-based ARDTs while also successfully capturing the changes in important AR characteristics such as mean **IVT** and the associated precipitation.

Extreme precipitation associated with ARs. Extreme precipitation (XP) is defined as daily precipitation greater than the 95th percentile of daily precipitation within the CESM UHR PD simulation and ERA5 reanalysis, respectively. In other words, the definition of extreme precipitation does not change between present and future scenarios. To examine the link between ARs and extreme precipitation events, we calculate the conditional probability of extreme precipitation given the presence of an AR, or $P(XP|AR)$. As expected, the presence of an AR leads to an increased probability of extreme precipitation everywhere (Fig. 4a, b). Notably, ERA5 and CESM UHR PD identify the same regions for the risk of AR-induced extreme precipitation, although the CESM UHR PD simulation slightly overestimates the probability of AR-induced extreme precipitation. The increased probability is most visible along the coastlines where ARs make landfall and the winds hit perpendicular to regions with a strong topographic gradient (Supplementary Fig. 16a). For example, there are some regions in which the presence of an AR makes precipitation 10 times more likely, such as over the southwestern coast of the U.S., western Greenland, and around the Antarctic coastline (Fig. 4a, b). Other hotspots for AR-induced extreme precipitation are the Iberian Peninsula, the Scandinavian mountains in Norway, the Andes mountains, the Ural mountains, the Hindukush mountains, western Australia, and western South Africa. Expansion of the subtropical dry belt in response to GHG warming leads to a regional reduction of mean precipitation and of AR-induced extreme precipitation in those regions (Fig. 4c–e, Supplementary Figs. 15 and 16). By contrast, the probability of extreme AR precipitation increases substantially on the poleward side of the subsidence regions. The largest increases are seen along the windward side of mountain ranges perpendicular to the large-scale circulation (Fig. 4c–e). To reiterate, ARs and associated mean and extreme precipitation play an important role in ice, precipitation, and cloud feedbacks, and better quantifying the impacts of AR-induced extreme precipitation events on sea ice, ice sheets and permafrost regions will be of paramount importance for future studies in understanding Earth's hydroclimatic response to GHG warming.

Conclusions
We combined the novelty of CESM UHR simulations and application of a novel, local geometric shape-based ARDT that is independent of **IVT** or IWV thresholds to estimate and analyze projected changes in AR characteristics. The results are consistent with previous studies indicating an increase in the mean
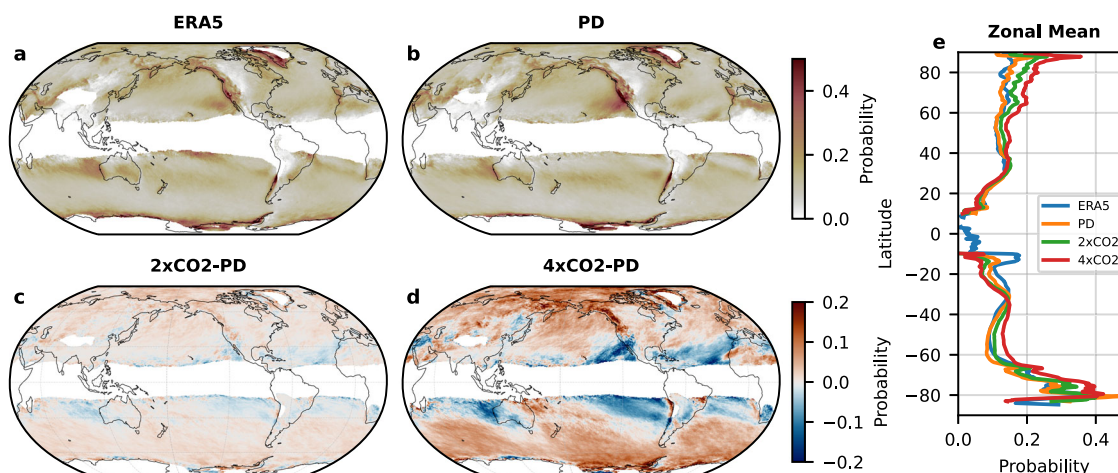
Fig. 4 Probability of extreme precipitation given an AR. Probability of extreme precipitation (95th percentile of daily mean precipitation) given the presence of an AR, P(XP|AR), for ERA5 (**a**) and CESM UHR PD simulation (**b**), respectively. Changes in the probability of AR-induced extreme precipitation for 2CO2 (**c**) and 4CO2 (**d**) simulations. The zonal mean of the probability with lines representing ERA5 reanalysis (blue), present day (orange), 2CO2 (green), and 4CO2 (red) simulations are plotted as **e**.

frequency (by 6% and 12%) and annual mean precipitation associated with ARs (by 6% and 15%) in response to increased atmospheric CO_2 concentrations (for 2CO2 and 4CO2 simulations). The mean precipitation increases within ARs match the mean hydrological sensitivity[77] while the maximum precipitation intensity shows similar changes as in other hydrometeorologically saturated conditions[78]. Owing to the increased atmospheric water vapor content under global warming, we also observe a strengthening of ARs (as measured by mean **IVT**) by 15%(6%/°C) and 34%(7%/°C) in 2CO2 and 4CO2 simulations respectively, approximately following the Clausius-Clapeyron scaling (7%/°C). This leads to a slight enlargement of ARs in warmer conditions, but, this enlargement is much smaller than what is reported in other studies using ARDTs based on historical thresholds[33,34].

Defining ARs from historical thresholds in a warmer and wetter world results in the identification of a much larger area of conglomerated AR events, with lower mean AR precipitation and strength compared to the threshold independent or relative or second-derivative threshold based methods. Furthermore, the application of historical thresholds to future warming scenarios corresponds to a reduction in the number of AR-like structures per time step, as multiple AR-like structures are clumped together in a single conglomerate against the backdrop of scopious, basin-wide increases in mean IVT. By comparison, detection methods based on relative thresholds or local-shape indicate ARs slightly increase in area but with a relatively large enhancement in AR strength and mean precipitation. Additionally, they also project a rise in the number of AR events per instant as AR structures are isolated from the elevated background mean state[34]. According to our analysis, changes in AR frequency identified using SCAFET are tightly linked to the mean circulation changes in response to increased GHG forcing. Moreover, the UHR simulations are expected to better resolve the synoptic scale circulation patterns compared to coarser resolution simulations. Our results also appear to capture the interaction of AR circulation systems with the landfalling topography. These aspects of UHR simulations help us to more reliably project and explain AR-associated precipitation characteristics. The accumulated, mean, and extreme precipitation associated with ARs increase in response to increased GHG concentrations. Combining estimated AR frequency and precipitation changes may inform future water

management policies as consensus builds on projected changes under global warming.

Importantly, the lack of coherence between **IVT** and IWV threshold-dependent detection methods fundamentally stems from the lack of a quantitative definition for ARs, though this is difficult to systematically apply globally and in perpetuity. To address the ambiguity in defining thresholds for ARs, we develop SCAFET and use the local geometric shape of **IVT** magnitude to detect strong local maxima and coherence within water vapor transport to identify AR-like conditions. Detection algorithms for cyclones, AFs, and other phenomena may encounter comparable challenges when attempting to estimate future changes in their frequency and the associated precipitation[79–81]. This is because they are also expected to be responsive to variations in the mean state, which presents exciting opportunities for further investigation and improvement. When analyzing synoptic-scale dynamics that overlie different mean states, especially between present and increased CO_2 scenarios, using a local shape-based feature extraction algorithm could be useful for building scientific consensus going forward. The ARDT introduced in this study is now expanded into a general feature extraction and tracking method framework allowing us to more objectively quantify (background-state independent) future changes in synoptic-scale phenomena[61].

Methods
ERA5 reanalysis. European Centre for Medium-Range Weather Forecasts (ECMWF) Reanalysis Version 5 (ERA5) data[82] is used to validate the capability of the CESM UHR PD simulation in capturing AR characteristics and associated precipitation in the present climate. We use daily mean data of zonal velocity (**U**), meridional velocity (**V**), and specific humidity (*Q*) from 1000 hPa to 300 hPa for calculating integrated water vapor transport (**IVT**) and daily mean precipitation (PRECT) for 20 years (2000–2019) with a horizontal resolution of 31 km and 37 vertical levels. **IVT** is a vector quantity given by,

$$\text{IVTx} = -\frac{1}{g} \int_{1000hPa}^{300hPa} q\mathbf{U}\,dp \qquad (1)$$

$$\text{IVTy} = -\frac{1}{g}\int_{1000hPa}^{300hPa} q\mathbf{V}dp \qquad (2)$$

$$|\mathbf{IVT}| = \sqrt{\text{IVTx}^2 + \text{IVTy}^2} \qquad (3)$$

Ultra-high-resolution CESM1.2.2 simulations. This study analyzes fully coupled ultra-high-resolution simulations of the Community Earth System Model[83] version 1.2.2 (CESM UHR) with 3 different CO_2 concentrations: (1) the present-day value (PD, $CO_2 = 367$ ppm), (2) double CO2 (2CO2, $CO_2 = 734$ ppm) and (3) quadruple CO2 (4CO2, $CO_2 = 1468$ ppm) to represent present climate and enhanced GHG conditions. All three simulations use the Community Atmosphere Model (CAM5)[84] with spectral element dynamic core at a horizontal resolution of around 0.25° and 30 vertical layers, and the Parallel Ocean Program version 2 (POP2)[85] at a horizontal resolution of 0.1° and 62 vertical levels as the atmosphere and ocean components, respectively. The land component is the Community Land Model version 4 (CLM4)[86], and the ice component is the Community Ice Code version 4 (CICE4)[87]. The configuration has been successfully used in many previous studies[44,62,65,88,89]. The PD simulation was run for 140 years, while 2CO2 and 4CO2 simulations were run for 100 years after branching out from PD at year 71. For AR detection, we use $\mathbf{U}$, $\mathbf{V}$, Q, and PRECT (same as ERA5) for the last 20 years of each simulation.

Scalable Feature Extraction and Tracking (SCAFET). Although there is a wide variety of peer-reviewed ARDTs[50], this study uses a novel local geometric shape-based method to identify ARs, with broader applications for extracting synoptic-scale features for different background states[61]. As discussed in the main text, the aim of the new method is to rethink how the thresholds are used for feature extraction. In contrast with many existing ARDTs, we use local geometric shape of a field to extract AR structures instead of applying $\mathbf{IVT}$ or IWV thresholds directly. The method uses Shape Index (SI), a measure of the local shape of a field irrespective of the magnitude or the total curvature to identify features of interest. We expect this method to reduce the sensitivity of the estimated AR response to global warming with regard to the types and values of the thresholds used, as unlike climate variable thresholds, shape-based thresholds are not empirically derived for each unique data set and mean state. The representative vector field used for AR detection is $\mathbf{IVT}$. The major steps in the algorithm are explained below. The result after the execution of each step is illustrated in Supplementary Fig. 16. The detected ARs compare very well with results obtained using existing ARDTs in representing not only the mean distribution (Supplementary Fig. 2) but also in event detection (Supplementary Fig. 18).

1. Scale-space Selection: The first step in the algorithm is to suppress variability in scales much smaller than the feature to be extracted. For atmospheric rivers, a simple, grid-aware Gaussian smoothing (see https://unidata.github.io/MetPy/latest/api/generated/metpy.calc.smooth_gaussian.html) suppresses variability smaller than 1000 kms.
2. Shape Index Extraction: In classical differential geometry, eigenvalues of the Hessian of a field are used to measure local curvature of the surface. Here, we use eigenvalues of the Hessian of $\mathbf{IVT}$ magnitude to construct a Shape Index (SI) depicting the local shape of the surface as follows[66].

$$SI = \frac{2}{\pi}tan^{-1}\left[\frac{k_2 + k_2}{k_2 - k_1}\right] \qquad (4)$$

Where k_1 and k_2 are the two eigenvalues satisfying $k_1 \geq k_2$ for the Hessian matrix of $|\mathbf{IVT}|$ given by,

$$\mathcal{H}(|\mathbf{IVT}|) = \begin{bmatrix} \frac{\partial^2|\mathbf{IVT}|}{\partial x^2} & \frac{\partial^2|\mathbf{IVT}|}{\partial x \partial y} \\ \frac{\partial^2|\mathbf{IVT}|}{\partial y \partial x} & \frac{\partial^2|\mathbf{IVT}|}{\partial y^2} \end{bmatrix} \qquad (5)$$

The SI is a unitless, bounded quantity between -1 to 1, independent of the absolute magnitude or resolution of the scalar field. This invariance is crucial as it ensures that the SI focuses solely on the nature of curvature, independent of its magnitude or size. A traditional ARDT may use the absolute magnitude[7] of the field or its curvature[58] to identify AR like structures while SI would characterize all ridge structures on the $|\mathbf{IVT}|$ as ARs. The basic philosophy of SI can be summarized as "all circles are circles regardless of its radius".The SI provides a single-value representation that captures different shapes: values close to -1 represent concave surfaces, values near +1 indicate convex shapes, and the intermediate range corresponds to transitional shapes like flat or saddle-shaped regions. This intuitive interpretation makes the SI an effective tool for characterizing and analyzing local shapes across a wide range of applications. To obtain AR-like structures, the SI threshold of 0.375 is chosen to extract local shapes such as ridges, caps, and domes. Additionally, points where the $\mathbf{IVT}$ deviates by more than 45° from the local ridge are also removed to ensure coherence in the transport direction. The local ridge is aligned in the direction of the eigenvector corresponding to k_2.

3. Filtering: A variety of geometric and physical characteristics of the objects obtained from the previous step are estimated. Later, weak structures are removed by fixing a minimum mean precipitation of 1mm/day for each object. Other filters are applied to eliminate small (area $< 2 \times 10^6 km^2$), short (length <2000km) and circular (eccentricity < 0.75) structures. AR-like structures associated with the Inter-Tropical Convergence Zone (ITCZ) are removed by masking out objects centered between 20°S and 20°N.
4. Tracking: The distance between filtered objects for each adjacent timestep is calculated based on their centroids. The closest objects among them are identified as the progression of one AR. If the distance traveled is greater than 4000km per day, the object is considered to be separate. Objects with a duration of less than two days are removed from the analysis.

IVT decomposition. IVTx is decomposed into mean and anomaly as follows

$$\begin{aligned} \text{IVTx} &= -\frac{1}{g}\int_{P_s}^{P_t} (\bar{q} + q')(\bar{u} + u')dp \\ &= -\frac{1}{g}\int_{P_s}^{P_t} \bar{q}\bar{u} + q'u' + \bar{q}u' + q'\bar{u}dp \end{aligned} \qquad (6)$$

Where $\bar{u}$, and $\bar{q}$ are the monthly mean zonal velocity and specific humidity respectively and u', and q' are anomalous zonal velocity and specific humidity with respect to monthly means. The pressure levels are integrated from $p_s = 1000$ hPa to $p_t = 300$ hPa. The same pressure bounds are also chosen for the IVT calculation in AR detection.

For a particular mean state, the time averaged IVTx is calculated as,

$$\overline{\text{IVTx}} = -\frac{1}{g}\int_{P_s}^{p_t} \overline{\bar{q}\bar{u}} + \overline{q'u'} + \overline{\bar{q}u'} + \overline{q'\bar{u}} \ dp$$

$$= -\frac{1}{g}\int_{P_s}^{p_t} \bar{q}\bar{u} + \overline{q'u'} \tag{7}$$

The change in $\overline{\text{IVTx}}$ between two mean states is calculated as,

$$\Delta\overline{\text{IVTx}} = \overline{\text{IVTx}}_2 - \overline{\text{IVTx}}_1$$

$$= -\frac{1}{g}\int_{P_s}^{p_t} \left[\bar{q}_2\bar{u}_2 + \overline{q'_2 u'_2} - \bar{q}_1\bar{u}_1 - \overline{q'_1 u'_1}\right] dp \tag{8}$$

Substituting $\bar{u}_2 = \bar{u}_1 + \Delta\bar{u}$, and $\bar{q}_2 = \bar{q}_1 + \Delta\bar{q}$ in Eq. (8)
We identify the dynamic, thermodynamic, and eddy terms as follows.

$$\Delta\overline{\text{IVTx}} = \overline{\text{IVTx}}_2 - \overline{\text{IVTx}}_1$$

$$= -\frac{1}{g}\int_{P_s}^{p_t} \left[(\bar{q}_1 + \Delta\bar{q})(\bar{u}_1 + \Delta\bar{u}) + \overline{q'_2 u'_2} - \bar{q}_1\bar{u}_1 + \overline{q'_1 u'_1}\right] dp$$

$$= -\underbrace{\frac{1}{g}\int_{P_s}^{p_t} \bar{q}_1\Delta\bar{u}dp}_{\substack{\text{Zonal component} \\ \text{of dynamic term}}} - \underbrace{\frac{1}{g}\int_{P_s}^{p_t} \bar{u}_1\Delta\bar{q}dp}_{\substack{\text{Zonal component} \\ \text{of thermodynamic term}}} - \underbrace{\frac{1}{g}\int_{P_s}^{p_t} \overline{q'_2 u'_2} - \overline{q'_1 u'_1} \ dp}_{\substack{\text{Zonal component} \\ \text{of eddy term}}}$$

$$\tag{9}$$

Similarly, IVTy is decomposed into dynamic, thermodynamic, and eddy terms as

$$\Delta\overline{\text{IVTy}} = \overline{\text{IVTy}}_2 - \overline{\text{IVTy}}_1$$

$$= -\frac{1}{g}\int_{P_s}^{p_t} \left[(\bar{q}_1 + \Delta\bar{q})(\bar{v}_1 + \Delta\bar{v}) + \overline{q'_2 v'_2} - \bar{q}_1\bar{v}_1 + \overline{q'_1 v'_1}\right] dp$$

$$= -\underbrace{\frac{1}{g}\int_{P_s}^{p_t} \bar{q}_1\Delta\bar{v}dp}_{\substack{\text{Meridional component} \\ \text{of dynamic term}}} - \underbrace{\frac{1}{g}\int_{P_s}^{p_t} \bar{v}_1\Delta\bar{q}dp}_{\substack{\text{Meridional component} \\ \text{of thermodynamic term}}} - \underbrace{\frac{1}{g}\int_{P_s}^{p_t} \overline{q'_2 v'_2} - \overline{q'_1 v'_1} \ dp}_{\substack{\text{Meridional component} \\ \text{of eddy term}}}$$

$$\tag{10}$$

Noting that for both zonal and meridional components, thermodynamic term > dynamic term ≫ eddy term, we can neglect the eddy terms. Now isolating thermodynamic and dynamic terms, we can write,

The thermodynamic component of **IVT** changes is formulated as,

$$\mathbf{TIVT} = \text{TIVTx}\hat{i} + \text{TIVTy}\hat{j}$$

$$= -\frac{1}{g}\int_{P_s}^{p_t} \bar{u}_1\Delta\bar{q}dp\hat{i} - \frac{1}{g}\int_{P_s}^{p_t} \bar{v}_1\Delta\bar{q}dp\hat{j} \tag{11}$$

The dynamic component of **IVT** changes is formulated as,

$$\mathbf{DIVT} = \text{DIVTx}\hat{i} + \text{DIVTy}\hat{j}$$

$$= -\frac{1}{g}\int_{P_s}^{p_t} \bar{q}_1\Delta\bar{u}dp\hat{i} - \frac{1}{g}\int_{P_s}^{p_t} \bar{q}_1\Delta\bar{v}dp\hat{j} \tag{12}$$

Finally, to express the **TIVT** and **DIVT** with respect to the PD mean **IVT**, we calculate the vector projection of each component onto **IVT**. This approach simplifies our analysis by illustrating the impact of each component on the mean **IVT** in the PD. Negative values indicate opposing effects on the PD **IVT**, whereas positive values signify strengthening of the mean **IVT** in the PD due to the specific vector being examined.

The vector projection of thermodynamic component (**TIVT**) onto **IVT** is calculated as,

$$\frac{\mathbf{TIVT} \cdot \mathbf{IVT}}{|\mathbf{IVT}|} \tag{13}$$

Likewise, the vector projection of dynamic component (**DIVT**) onto **IVT** is calculated as,

$$\frac{\mathbf{DIVT} \cdot \mathbf{IVT}}{|\mathbf{IVT}|} \tag{14}$$

Data availability

Code availability

References

1. Ralph, F. M., Dettinger, M. D., Cairns, M. M., Galarneau, T. J. & Eylander, J. Defining "atmospheric river": How the glossary of meteorology helped resolve a debate. *Bull. Am. Meteorol. Soc.* **99**, 837–839 (2018).
2. Zhu, Y. & Newell, R. E. Atmospheric rivers and bombs. *Geophys. Res. Lett.* **21**, 1999–2002 (1994).
3. Zhu, Y. & Newell, R. E. A proposed algorithm for moisture fluxes from atmospheric rivers. *Mon. Weather Rev.* **126**, 725–735 (1998).
4. Nash, D., Waliser, D., Guan, B., Ye, H. & Ralph, F. M. The role of atmospheric rivers in extratropical and polar hydroclimate. *J. Geophys. Res. Atmos.* **123**, 6804–6821 (2018).
5. Shields, C. A. et al. Meridional heat transport during atmospheric rivers in high-resolution CESM climate projections. *Geophys. Res. Lett.* **46**, 14702–14712 (2019).
6. Payne, A. E. et al. Responses and impacts of atmospheric rivers to climate change. *Nat. Rev. Earth Environ.* **1**, 143–157 (2020).
7. Guan, B. & Waliser, D. E. Detection of atmospheric rivers: evaluation and application of an algorithm for global studies. *J. Geophys. Res. Atmos.* **120**, 12514–12535 (2015).
8. Waliser, D. & Guan, B. Extreme winds and precipitation during landfall of atmospheric rivers. *Nat. Geosci.* **10**, 179–183 (2017).
9. Chen, X. et al. Predictability of extreme precipitation in western u.s. watersheds based on atmospheric river occurrence, intensity, and duration. *Geophys. Res. Lett.* **45**, 11–693 (2018).
10. Moore, B. J., Neiman, P. J., Ralph, F. M. & Barthold, F. E. Physical processes associated with heavy flooding rainfall in nashville, tennessee, and vicinity during 1–2 may 2010: The role of an atmospheric river and mesoscale convective systems. *Mon. Weather Rev.* **140**, 358–378 (2012).
11. Ralph, F. M. et al. Flooding on california's russian river: role of atmospheric rivers. *Geophys. Res. Lett.* **33**, https://doi.org/10.1029/2006GL026689 (2006).

12. Neiman, P. J., Ralph, F. M., Wick, G. A., Lundquist, J. D. & Dettinger, M. D. Meteorological characteristics and overland precipitation impacts of atmospheric rivers affecting the west coast of north america based on eight years of SSM/i satellite observations. *J. Hydrometeorol.* **9**, 22–47 (2008).

13. Lavers, D. A. et al. Winter floods in britain are connected to atmospheric rivers. *Geophys. Res. Lett.* **38**, n/a–n/a (2011).

14. Lavers, D. A. & Villarini, G. The nexus between atmospheric rivers and extreme precipitation across europe. *Geophys. Res. Lett.* **40**, 3259–3264 (2013).

15. Lavers, D. A. & Villarini, G. The contribution of atmospheric rivers to precipitation in europe and the united states. *J. Hydrol.* **522**, 382–390 (2015).

16. Viale, M. & Nuñez, M. N. Climatology of winter orographic precipitation over the subtropical central andes and associated synoptic and regional characteristics. *J. Hydrometeorol.* **12**, 481–507 (2011).

17. Chen, J., Zhang, H., Ye, C., Chen, H. & Mo, R. Case studies of atmospheric rivers over china and australia: new insight into their rainfall generation. *J. Southern Hemisphere Earth Syst. Sci.* **70**, 17 (2020).

18. Liang, P., Dong, G., Zhang, H., Zhao, M. & Ma, Y. Atmospheric rivers associated with summer heavy rainfall over the yangtze plain. *J. Southern Hemisphere Earth Syst. Sci.* **70**, 54 (2020).

19. Pan, M. & Lu, M. East asia atmospheric river catalog: annual cycle, transition mechanism, and precipitation. *Geophys. Res. Lett.* **47**, e2020GL089477 (2020).

20. Yang, Y., Zhao, T., Ni, G. & Sun, T. Atmospheric rivers over the bay of bengal lead to northern indian extreme rainfall. *Int. J. Climatol.* **38**, 1010–1021 (2017).

21. Goldenson, N., Leung, L. R., Bitz, C. M. & Blanchard-Wrigglesworth, E. Influence of atmospheric rivers on mountain snowpack in the western united states. *J. Clim.* **31**, 9921–9940 (2018).

22. Guan, B., Molotch, N. P., Waliser, D. E., Fetzer, E. J. & Neiman, P. J. Extreme snowfall events linked to atmospheric rivers and surface air temperature via satellite measurements. *Geophys. Res. Lett.* **37**, n/a–n/a (2010).

23. Huning, L. S., Guan, B., Waliser, D. E. & Lettenmaier, D. P. Sensitivity of seasonal snowfall attribution to atmospheric rivers and their reanalysis-based detection. *Geophys. Res. Lett.* **46**, 794–803 (2019).

24. Little, K., Kingston, D. G., Cullen, N. J. & Gibson, P. B. The role of atmospheric rivers for extreme ablation and snowfall events in the southern alps of new zealand. *Geophys. Res. Lett.* **46**, 2761–2771 (2019).

25. Lora, J. M., Mitchell, J. L., Risi, C. & Tripati, A. E. North pacific atmospheric rivers and their influence on western north america at the last glacial maximum. *Geophys. Res. Lett.* **44**, 1051–1059 (2017).

26. Skinner, C. B., Lora, J. M., Payne, A. E. & Poulsen, C. J. Atmospheric river changes shaped mid-latitude hydroclimate since the mid-holocene. *Earth Planet. Sci. Lett.* **541**, 116293 (2020).

27. Tabor, C. et al. A mechanistic understanding of oxygen isotopic changes in the western united states at the last glacial maximum. *Quat. Sci. Rev.* **274**, 107255 (2021).

28. Gorodetskaya, I. V. et al. The role of atmospheric rivers in anomalous snow accumulation in east antarctica. *Geophys. Res. Lett.* **41**, 6199–6206 (2014).

29. Wille, J. D. et al. West antarctic surface melt triggered by atmospheric rivers. *Nat. Geosci.* **12**, 911–916 (2019).

30. Francis, D., Mattingly, K. S., Temimi, M., Massom, R. & Heil, P. On the crucial role of atmospheric rivers in the two major weddell polynya events in 1973 and 2017 in antarctica. *Sci. Adv.* **6**, eabc2695 (2020).

31. Hegyi, B. M. & Taylor, P. C. The unprecedented 2016-2017 arctic sea ice growth season: the crucial role of atmospheric rivers and longwave fluxes. *Geophys. Res. Lett.* **45**, 5204–5212 (2018).

32. Mattingly, K. S., Mote, T. L. & Fettweis, X. Atmospheric river impacts on greenland ice sheet surface mass balance. *J. Geophys. Res. Atmos.* **123**, 8538–8560 (2018).

33. Espinoza, V., Waliser, D. E., Guan, B., Lavers, D. A. & Ralph, F. M. Global analysis of climate change projection effects on atmospheric rivers. *Geophys. Res. Lett.* **45**, 4299–4308 (2018).

34. O'Brien, T. A. et al. Increases in future AR count and size: overview of the ARTMIP tier 2 CMIP5/6 experiment. *J. Geophys. Res. Atmos.* **127**, e2021JD036013 (2022).

35. Gershunov, A. et al. Precipitation regime change in western north america: the role of atmospheric rivers. *Sci. Rep.* **9**, 9944 (2019).

36. Rhoades, A. M. et al. The shifting scales of western u.s. landfalling atmospheric rivers under climate change. *Geophys. Res. Lett.* **47**, e2020GL089096 (2020).

37. Rhoades, A. M., Risser, M. D., Stone, D. A., Wehner, M. F. & Jones, A. D. Implications of warming on western united states landfalling atmospheric rivers and their flood damages. *Weather Clim. Extremes* **32**, 100326 (2021).

38. Patricola, C. M. et al. Future changes in extreme precipitation over the san francisco bay area: dependence on atmospheric river and extratropical cyclone events. *Weather Clim. Extremes* **36**, 100440 (2022).

39. Guan, B. & Waliser, D. E. Atmospheric rivers in 20 year weather and climate simulations: a multimodel, global evaluation. *J. Geophys. Res. Atmos.* **122**, 5556–5581 (2017).

40. Harvey, B. J., Cook, P., Shaffrey, L. C. & Schiemann, R. The response of the northern hemisphere storm tracks and jet streams to climate change in the CMIP3, CMIP5, and CMIP6 climate models. *J. Geophys. Res. Atmos.* **125**, e2020JD032701 (2020).

41. Yim, B. Y., Min, H. S. & Kug, J.-S. Inter-model diversity in jet stream changes and its relation to arctic climate in CMIP5. *Clim. Dyn.* **47**, 235–248 (2015).

42. Hagos, S., Leung, L. R., Yang, Q., Zhao, C. & Lu, J. Resolution and dynamical core dependence of atmospheric river frequency in global model simulations. *J. Clim.* **28**, 2764–2776 (2015).

43. Delworth, T. L. et al. Simulated climate and climate change in the GFDL CM2.5 high-resolution coupled climate model. *J. Clim.* **25**, 2755–2781 (2012).

44. Small, R. J. et al. A new synoptic scale resolving global climate simulation using the community earth system model. *J. Adv. Model. Earth Syst.* **6**, 1065–1094 (2014).

45. Swenson, E. T., Lu, J. & Straus, D. M. Resolution dependence and rossby wave modulation of atmospheric rivers in an aquaplanet model. *J. Geophys. Res.* **123**, 6297–6311 (2018).

46. Bryan, F. O. et al. Frontal scale air–sea interaction in high-resolution coupled climate models. *J. Clim.* **23**, 6277–6291 (2010).

47. Salathé, E. P., Steed, R., Mass, C. F. & Zahn, P. H. A high-resolution climate model for the u.s. pacific northwest: Mesoscale feedbacks and local responses to climate change. *J. Clim.* **21**, 5708–5726 (2008).

48. O'Brien, T. A. et al. Detection of atmospheric rivers with inline uncertainty quantification: TECA-BARD v1.0.1. *Geosci. Model Dev.* **13**, 6131–6148 (2020).

49. Lora, J. M., Shields, C. A. & Rutz, J. J. Consensus and disagreement in atmospheric river detection: ARTMIP global catalogues. *Geophys. Res. Lett.* **47**, e2020GL089302 (2020).

50. Shields, C. A. et al. Atmospheric river tracking method intercomparison project (ARTMIP): project goals and experimental design. *Geosci. Model Dev.* **11**, 2455–2474 (2018).

51. Climate, N. & (CGD), G. D. Algorithms, atmospheric river tracking method intercomparison project (artmip) https://www.cgd.ucar.edu/projects/artmip/algorithms (2019).

52. Rutz, J. J., Steenburgh, W. J. & Ralph, F. M. Climatological characteristics of atmospheric rivers and their inland penetration over the western united states. *Month. Weather Rev.* **142**, 905–921 (2014).

53. Sellars, S. L., Gao, X. & Sorooshian, S. An object-oriented approach to investigate impacts of climate oscillations on precipitation: a western United States case study. *J. Hydrometeorol.* **16**, 830–842 (2015).

54. Ullrich, P. A. et al. TempestExtremes v2.1: a community framework for feature detection, tracking and analysis in large datasets. *Geosci. Model Dev.* **14**, 5023–5048 (2021).

55. Mundhenk, B. D., Barnes, E. A. & Maloney, E. D. All-season climatology and variability of atmospheric river frequencies over the north pacific. *J. Clim.* **29**, 4885–4903 (2016).

56. Pan, M. & Lu, M. A novel atmospheric river identification algorithm. *Water Resour. Res.* **55**, 6069–6087 (2019).

57. Zhao, M. Simulations of atmospheric rivers, their variability, and response to global warming using GFDL's new high-resolution general circulation model. *Journal of Climate* **33**, 10287–10303 (2020).

58. Ullrich, P. A. & Zarzycki, C. M. TempestExtremes: a framework for scale-insensitive pointwise feature tracking on unstructured grids. *Geosci. Model Dev.* **10**, 1069–1090 (2017).

59. Muszynski, G., Kashinath, K., Kurlin, V. & and, M. W. Topological data analysis and machine learning for recognizing atmospheric river patterns in large climate datasets. *Geosci. Model Dev.* **12**, 613–628 (2019).

60. Xu, G., Ma, X., Chang, P. & Wang, L. Image-processing-based atmospheric river tracking method version 1 (IPART-1). *Geosci. Model Dev.* **13**, 4639–4662 (2020).

61. Nellikkattil, A. B., OB´rien, T. A., Lemmon, D., Lee, J.-Y. & Chu, J.-E. *Scalable feature extraction and tracking (SCAFET): a general framework for feature extraction from large climate datasets* (EGUsphere, 2023).

62. Chu, J.-E. et al. Reduced tropical cyclone densities and ocean effects due to anthropogenic greenhouse warming. *Sci. Adv.* **6**, eabd5109 (2020).

63. Collow, A. B. M. et al. An overview of ARTMIP's tier 2 reanalysis intercomparison: Uncertainty in the detection of atmospheric rivers and their associated precipitation. *J. Geophys. Res. Atmos.* **127**, e2021JD036155 (2022).

64. Shields, C. A. et al. Future atmospheric rivers and impacts on precipitation: Overview of the ARTMIP tier 2 high resolution global warming experiment. *Geophys. Res. Lett.* **50**, e2022GL102091 (2023).

65. Chang, P. et al. An unprecedented set of high-resolution earth system simulations for understanding multiscale interactions in climate variability and change. *J. Adv. Model. Earth Syst.* **12**, e2020MS002298 (2020).

66. Koenderink, J. J. & van Doorn, A. J. Surface shape and curvature scales. *Image Vis. Comput.* **10**, 557–564 (1992).

67. Eckhardt, S. et al. A 15-year climatology of warm conveyor belts. *J. Clim.* **17**, 218–237 (2004).

68. Hoskins, B. J. & Hodges, K. I. New perspectives on the northern hemisphere winter storm tracks. *J. Atmos. Sci.* **59**, 1041–1061 (2002).
69. Hoskins, B. J. & Hodges, K. I. A new perspective on southern hemisphere storm tracks. *J. Clim.* **18**, 4108–4129 (2005).
70. Berry, G., Reeder, M. J. & Jakob, C. A global climatology of atmospheric fronts. *Geophys. Res. Lett.* **38**, n/a–n/a (2011).
71. Dacre, H. F., Clark, P. A., Martinez-Alvarado, O., Stringer, M. A. & Lavers, D. A. How do atmospheric rivers form? *Bull. Am. Meteorol. Soc.* **96**, 1243–1255 (2015).
72. Dacre, H. F., Martínez-Alvarado, O. & Mbengue, C. O. Linking atmospheric rivers and warm conveyor belt airflows. *J. Hydrometeorol.* **20**, 1183–1196 (2019).
73. Zhang, Z., Ralph, F. M. & Zheng, M. The relationship between extratropical cyclone strength and atmospheric river intensity and position. *Geophys. Res. Lett.* **46**, 1814–1823 (2019).
74. Guo, Y., Shinoda, T., Guan, B., Waliser, D. E. & Chang, E. K. M. Statistical relationship between atmospheric rivers and extratropical cyclones and anticyclones. *J. Clim.* **33**, 7817–7834 (2020).
75. Held, I. M. & Soden, B. J. Robust responses of the hydrological cycle to global warming. *J. Clim.* **19**, 5686–5699 (2006).
76. McClenny, E. E., Ullrich, P. A. & Grotjahn, R. Sensitivity of atmospheric river vapor transport and precipitation to uniform sea surface temperature increases. *J. Geophys. Res. Atmos.* **125**, e2020JD033421 (2020).
77. Douville, H. et al. *Water Cycle Changes*, 1055–1210 (Cambridge University Press, Cambridge, United Kingdom and New York, NY, USA, 2021).
78. Stansfield, A. M. & Reed, K. A. Global tropical cyclone precipitation scaling with sea surface temperature. *npj Clim. Atmos. Sci.* **6**, 60 (2023).
79. Neu, U. et al. IMILAST: A community effort to intercompare extratropical cyclone detection and tracking algorithms. *Bull. Am. Meteorol. Soc.* **94**, 529–547 (2013).
80. Zarzycki, C. M. & Ullrich, P. A. Assessing sensitivities in algorithmic detection of tropical cyclones in climate data. *Geophys. Res. Lett.* **44**, 1141–1149 (2017).
81. Bourdin, S., Fromang, S., Dulac, W., Cattiaux, J. & Chauvin, F. Intercomparison of four algorithms for detecting tropical cyclones using ERA5. *Geosci. Model Dev.* **15**, 6759–6786 (2022).
82. Hersbach, H. et al. The ERA5 global reanalysis. *Q. J. R. Meteorol. Soc.* **146**, 1999–2049 (2020).
83. Hurrell, J. W. et al. The community earth system model: a framework for collaborative research. *Bull. Am. Meteorol. Soc.* **94**, 1339–1360 (2013).
84. Neale, R. B. et al. *Description of the NCAR community atmosphere model (CAM 5.0)* NCAR Tech. Note NCAR/TN-486+ STR 1, 1–12 (NCAR, 2010).
85. Smith, R. & Gent, P. *Reference manual for the parallel ocean program (pop)*. Los Alamos unclassified report LA-UR-02-2484 (Los Alamos, 2002).
86. Lawrence, D. M. et al. Parameterization improvements and functional and structural advances in version 4 of the community land model. *J. Adv. Model. Earth Syst.* **3**, n/a–n/a (2011).
87. Hunke, E. C., Lipscomb, W. H., Turner, A. K., Jeffery, N. & Elliott, S. *Cice: the Los Alamos sea ice model documentation and software user's manual, version 4.1. la-cc-06-012* **675**, 500 (T-3 Fluid Dynamics Group, Los Alamos National Laboratory, 2010).
88. Wengel, C. et al. Future high-resolution el niño/southern oscillation dynamics. *Nat. Clim. Change* **11**, 758–765 (2021).
89. Wang, S. et al. El niño/southern oscillation inhibited by submesoscale ocean eddies. *Nat. Geosci.* **15**, 112–117 (2022).

Acknowledgements

Author contributions

A.B.N., J-Y. L., and A.T. designed the study. A.B.N. conducted the data analysis and prepared the figures. S-S.L. conducted the CESM UHR simulations. D.L. designed the IVT decomposition method which was implemented with assistance from A.B.N. and J-E.C. B.G. supervised the development the feature detection method and provided useful benchmarks. A.B.N., J-Y. L., and D.L. wrote the initial manuscript draft. All authors contributed to the interpretation of the results and to the improvement of the manuscript.

Competing interests

The authors declare no competing interests.

Additional information